On the design of thermal management systems for hybrid-electric aircraft

Maria Coutinho
maria.coutinho@tecnico.ulisboa.pt

Instituto Superior Técnico, Universidade de Lisboa, Portugal

December 2022

Abstract

The electrification of aircraft propulsive system is identified as a potential solution towards a lower carbon footprint in the aviation industry. One of the effects of increased electrification is the generation of a large amount of waste heat that needs to be removed. As high-power systems must be cooled to avoid performance deterioration such as battery thermal runaway, a suitable thermal management system is required to regulate the thermal behaviour of the powertrain components. With this in mind, the main objective of this research is to identify promising heat transfer technologies to be integrated into a Thermal Management System (TMS) such that power, mass, and drag can be minimised for a parallel hybrid-electric regional aircraft in the context of an EU-funded FutPrInt50 project. Five different TMS architectures are modelled using the Matlab/Simulink environment based on thermodynamic principles, heat transfer fundamentals, and fluid flow equations. The systems are a combination of a closed-loop liquid cooling integrated with different heat dissipation components, namely ram air, skin heat exchanger, and fuel. Their cooling capacity and overall aircraft performance penalties under different flight conditions are estimated and compared to each other. Then, a parametric study is conducted, followed by a multi-objective robust optimisation analysis with the aim of minimising the TMS impact. None of the investigated architectures exhibits an ideal performance across the range of the studied metrics. The research revealed that while planning the TMS for future hybrid-electric aircraft, alternative architectures will have to be developed and studied in light of the power requirements.

Keywords: thermal management system, hybrid propulsion, multi-objective optimisation, skin heat exchanger, ram air, fuel

1. Introduction

The aviation sector is currently facing new challenges such as energy demand and environmental impact. The report *"Flightpath 2050 : Europe's vision for future aviation"* set several goals that must be accomplished by the year 2050 [1], including a reduction in 75% of CO_2 emissions. In this context, sustainable multidisciplinary design is quickly becoming a key factor in the development of the next generation aircraft [2].

In this multidisciplinary analysis, the interaction of propulsion and energy fields is of particular interest. Using electric powertrains and cleaner energy sources as a propulsive system seems to be a promising solution [2]. However, more electric aircraft have increased demands on engines for thrust and power generation, leading to hotter fluids, higher component temperatures and increased heat generation [3]. Although electrical equipment is typically efficient, the large amount of electrical power needed (in the Megawatt range) will result in significant power losses. Additionally, the heat created by the electric propulsion system cannot be taken through the engine nozzles and the use of ram air to cool electric systems is limited because of their greater integration into the fuselage [3]. There is also a increased risk of thermal runaway with some systems, especially batteries [3]. Thus, novel Thermal Management Systems (TMSs) are required and may be designed in parallel with the Hybrid-Electric Propulsion (HEP) architecture. The TMS will be responsible for regulating the temperature of the aircraft subsystems/components by managing heat transfer between heat sources and heat sinks in order to optimise comfort, safety, and efficiency [4]. Therefore, the TMS major goal is to maximise the use of heat produced and, at the same time, allow diverse components and systems to run within a safe temperature range.

Within this framework, the FutPrint50 project stands out as a critical endeavour aimed at discovering and developing technologies and combinations that will help to speed up the entry-into-service to 2035/2040 of commercial regional Hybrid-Electric Aircraft (HEA) [5]. The main goal of this research work, as a FutPrInt50 collaboration, is to study new and existing heat dissipation systems and develop possible TMS architectures. This will help to understand the influence of a TMS on the power, weight, and drag and study the feasibility of these architectures in future aircraft.

2. Literature review

2.1. Overview of heat transfer technologies

The thermal management system acquires heat at the **heat source**, **transport** it to a specialised heat sink, and rejects it at the **heat sink** [3]. Understanding the **heat source** behaviour is thus essential since it influences TMS requirements. Heat sources are any component or system that generates heat, either as a byproduct or as its main function. Electrified propulsion systems are expected to generate additional heat loads beyond combustion engines, mechanical power transmission, and the Environment Control System (ECS). Main electric powertrain heat sources may include electric motors/generators, batteries, fuel cells and power converters/distributors. The

thermal **transport** system will be responsible for the heat transfer until the specialised heat sink. Heat exchangers, liquid cooling loops and refrigeration cooling loops, namely Vapour Compression Systems (VCS) can be used in this stage. The **heat sink** absorbs the thermal source heat. Given their high Technology Readiness Level (TRL) in aircraft [4], atmospheric air and fuel are the main terminal heat sinks:

Atmospheric air Ram Air (RA), Engine Fan Air (EFA), and Skin Heat Exchanger (SHX) may be utilised as atmospheric air heat sinks. **RA** systems use the dynamic pressure caused by the movement of the aircraft to ingest air into a duct that can be charged directly to cool down the devices or can be transferred to Ram Air Heat Exchangers (RHXs) to cool down a coolant. In ram air inlets, the air is brought to a halt relative to the aircraft which causes significant drag. **EFA** systems usually employ compressed air from the compressor stage of a gas turbine to cool the downstream engine components or maintain cabin temperature and pressure. It eliminates the apertures outside the aircraft that RA systems need, but it has reduced cooling capacity. **SHX** system uses the aircraft surface to reach the atmospheric air heat sink. The heated fluid contacts the air-frame skin, which contacts the ambient air via surface heat exchangers. This reduces air inlets, minimising RA system cooling drag [6].

Fuel Aircraft fuel is abundant and easily transported, making it a common heat sink. Besides, hydrocarbon fuels have, in general, better heat transfer properties than air, making them a more effective cooling fluid [3]. At the same time there is a thermodynamic advantage of preheating fuel before combustion resulting in a more efficient thermal cycle. Using fuel also has its drawbacks, including fuel stability and fuel thermal endurance that can affect the aircraft safety. In the ultimate case of a fully electric aeroplane, no fuel will be available on-board. Thus, reducing the heat loads from the Fuel Thermal Management System (FTMS) itself and improving its thermal behaviour is of extreme importance.

2.2. Overview of TMS architectures

Most of the technologies previously described are used in the current research on TMS for electrified aircraft propulsion. The challenge is the effective interaction of the different heat sources, cooling loops and heat sinks to increase the overall TMS performance. Table 1 sums up some of the most important studies on the TMS integration conducted recently [7–15]. These studies suggest that liquid cooling, ram air cooling, outer mould line cooling, heat exchangers, and the use of fuel as a heat sink are the most promising heat transfer systems. Most of the TMS configurations studied were based on liquid-ram air cooling loops. A coolant with a high thermal capacity, such as PGW30, or PSF-5 is required. The use of Sustainable Aviation Fuel (SAF) instead of Jet-A both on the powerplant and as a heat sink can also bring advantages. Firstly, due to the high degree of uniformity across current aircraft, engines, and fuel standards. Secondly, because life cycle carbon emissions can be reduced [16].

Table 1: Research TMS architectures.

Aircraft(PAX)	Cooling system	Ref.
ECO-150R(150)	RA and liquid	[7]
STARC-ABL(154)	EFA, RA, fuel, liquid (oil+PGW30/PSF-5) and SHX	[8, 9]
PEGASUS(48)	RA, liquid (PGW30/PSF-5) and SHX	[8, 9]
SUSAN(180)	RA, fuel, liquid (PGW30/PSF-5) and SHX	[10]
ULI(76)	RA, ECS air and liquid	[11]
Short-range aircraft(180)	RA	[12]
Short-range aircraft(180)	Fuel tank with internal heating and SHX	[13]
Notional aircraft	FTMS (single and dual tank topology)	[14, 15]

3. Methodology

3.1. Reference aircraft and mission

The base propulsion architecture used to design and size the TMS is a parallel hybrid architecture with two turboprop engines running on SAF and coupled to an electric motor each, that can be also powered by battery packs. Wingtip propellers driven by electric motors enhance the powerplant. The TMS should regulate the temperature of the different components in the described powerplant. With this in mind, the total waste heat load generated by these components and their operating temperatures were estimated. The estimations showed that the critical heat waste load occurs during the take-off phase (237 kW). The TMS will be designed to manage half of the total heat load according to the symmetry of the HEP architecture. A round number of 100 kW (200 kW/ 2) is considered a generic heat load ($\dot{Q}_{\text{equip}}$). An assumed value of 100 kW (200 kW/ 2) is considered as a generic heat load ($\dot{Q}_{\text{equip}}$). The operating temperature of the battery pack limits the heat load intake liquid temperature (control temperature). Regarding the reference mission, a range of 400 km, a cruise speed of 520 km/h and a cruise altitude of 7010 m were considered.

3.2. TMS Architectures

Five TMS architectures are modelled using the most promising heat transfer technologies identified in the literature review. Architecture 1 **(A1)** and Architecture 2 **(A2)** both use a liquid cooling loop, a VCS and a RA inlet to cool the equipment. The difference between the two is that, in A1, the heat is only removed via the evaporator to the VCS, while, in A2, before transferring heat to the VCS, the liquid rejects heat to the ambient air through a SHX. For sake of brevity, only A2 is shown in Figure 1.

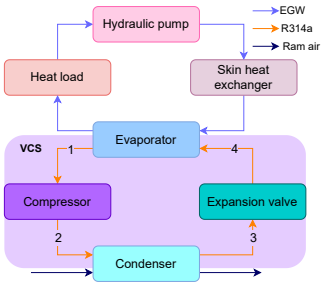

Figure 1: Proposed TMS Architecture 2.

Architecture 3 **(A3)** and Architecture 4 **(A4)** use a liquid cooling loop and RA inlet to cool the equipment. In A3, the liquid cooling loop only includes a heat rejection

station (RHX), while in architecture 4, before rejecting heat to a RA mass flow, the liquid transfers heat to the ambient air through a SHX. It is possible to note that case A3 basically corresponds to A1 but it replaces the VCS with a RHX, while A4 matches A2 but again replacing VCS with a RHX. Again for sake of brevity, just A4 is presented in Figure 2.

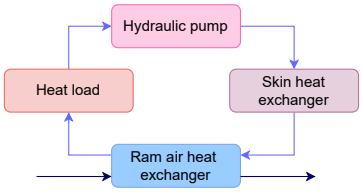

Figure 2: Proposed TMS Architecture 4.

Architecture 5 **(A5)**, depicted in Figure 3, differs from the others since it also uses fuel as a heat sink. To use fuel as a heat sink, a FTMS is developed and the fuel is heated via a fuel heat exchanger (FHX) and cooled using the skin heat exchanger concept.

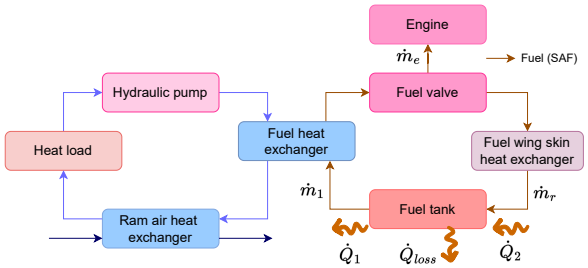

Figure 3: Proposed TMS Architecture 5.

3.3. Component model

The model equations for thermal balance and mass estimation were developed for each component that integrates the TMS architectures using Matlab/Simulink.

Heat load Heat load represents all the equipment to be cooled and it is provided to the system as a heat transfer rate $\dot{Q}_{equip}$. The first law of thermodynamics (principle of conservation of energy) applied to a control volume with fluid crossing its boundary adapted to a simplified steady-flow thermal system may determine the coolant output temperature [17]:

$$\dot{Q}_{\text{equip}} = \dot{m}_{\text{liquid}} \cdot c_p \cdot (T_{\text{liquid,o}} - T_{\text{control}}), \tag{1}$$

where c_p is the specific heat at constant pressure and T the liquid temperature. The i and o subscripts distinguish between fluid entry and exit, respectively. To compute the liquid mass flow rate ($\dot{m}_{\text{liquid}}$) a norm from a Society of Automotive Engineers report is used [18]. For liquid cooled avionics, flow rates range from 0.023 kg/s to 0.045 kg/s per kW are usually considered for coolants such as Ethylene-Glycol Water (EGW) mixtures.

Hydraulic and fuel pump Both EGW and fuel pump compensate for all fluid pressure drop (Δp), from the EGW/fuel passage through the ducts, heat loads, and heat sinks. Assuming a constant efficiency (η_{pump}) and knowing the fluid density (ρ_{liquid}), the pump power consumption W_{pump} may be estimated:

$$W_{\text{pump}} = \frac{\dot{m}_{\text{liquid}} \cdot \Delta p}{\rho_{\text{liquid}} \cdot \eta_{\text{pump}}}. \tag{2}$$

Heat exchangers The primary variables of a heat exchanger (HEX) are its heat transfer rate $\dot{Q}_{\text{HEX}}$ [W], surface exchanger area A_{HEX} [m^2], heat capacity rates $C(\dot{m} \cdot c_p)$ [W/K] and total heat transfer coefficient U [W/Km^2]. To determine the heat transfer rate, the steady flow energy equation is applied on hot and cold fluid sides and combined to an extension of Newton's law of cooling using the global heat transfer coefficient U and an adequate mean temperature difference T_{lm}. The system of three equations is set as follows:

$$\begin{cases} \dot{Q}_{\text{HEX}} = \dot{m}_h \cdot c_{p,h} \cdot (T_{h,i} - T_{h,o}) \\ \dot{Q}_{\text{HEX}} = \dot{m}_c \cdot c_{p,c} \cdot (T_{c,o} - T_{c,i}) \\ \dot{Q}_{\text{HEX}} = U \cdot A_{\text{HEX}} \cdot \Delta T_{\text{lm}} \end{cases} \tag{3}$$

where the subscripts h and c distinguish between hot and cold fluids, respectively, and A_{HEX} denotes the contact surface between a fluid and a wall. The appropriate average temperature difference is given by the Log Mean Temperature Difference (LMTD) method [17]:

$$\Delta T_{\text{lm}} = \frac{\Delta T_2 - \Delta T_1}{\ln(\Delta T_2 / \Delta T_1)}, \tag{4}$$

where ΔT_1 and ΔT_2 represent the terminal temperature differences between the two fluids. A counter-flow heat exchanger is chosen since it has a higher log mean temperature difference for identical intake and outtake temperatures than parallel flow HEX.

The ram air-EGW and fuel-EGW HEXs are designed using this approach with 10 K for $\Delta T1$ to guarantee a good heat transfer between the fluids. The total heat transfer surface area (A_{HEX}) is essential for a conceptual heat exchanger mass estimate. The detailed calculation of the global heat transfer coefficient was not considered in this project and reference overall heat transfer coefficients for the different flows are used [17]. Using the result values of (UA_{HEX}) and a reference U, the surface area can be estimated (A_{HEX}). Assuming compact heat exchangers [19, 20], their mass (m_{HEX}) and volume (V_{HEX}) are obtained according to the following equations, respectively:

$$m_{\text{HEX}} = \rho_{\text{HEX}} \cdot V_{\text{HEX}} \cdot (1 - \sigma), \tag{5}$$

$$V_{\text{HEX}} = \frac{A_{\text{HEX}}}{\beta}. \tag{6}$$

In the above expressions, the porosity factor (σ) and surface density (β) values are estimated based on provided references [19].

RA inlet/outlet and fan A ram air intake and outtake is employed to gather the needed air flow and expel it to the ambient. The standard ideal isentropic relations are used to compute the ram air pressure and temperatures [21]:

$$T_{\text{ram,i}} = T_\infty \cdot \left(1 + \frac{\gamma - 1}{2} \cdot M_\infty^2\right), \tag{7}$$

$$p_{\text{ram,i}} = p_\infty \cdot \left(1 + \frac{\gamma - 1}{2} \cdot M_\infty^2\right)^{\frac{\gamma}{\gamma-1}}, \tag{8}$$

$$M_{\text{ram,o}} = \sqrt{\frac{2}{\gamma - 1}\left[\left(\frac{p_{\text{RHX,o}}}{p_\infty}\right)^{\frac{\gamma-1}{\gamma}} - 1\right]}, \tag{9}$$

$$T_{\text{ram,o}} = \frac{T_{\text{RHX,o}}}{1 + \frac{\gamma-1}{2} M_{\text{ram,o}}^2}, \tag{10}$$

$$v_{\text{ram,o}} = M_{\text{ram,o}} \cdot \sqrt{T_{\text{ram,o}} \cdot \gamma \cdot R}, \tag{11}$$

where $T_{\text{RHX,o}}$ and $p_{\text{RHX,o}}$ represent the air temperature and pressure, respectively, when exiting the RHX, γ is the ratio of specific heat, R is the gas constant (287 J/kgK) and M_∞ is the Mach number of the aeroplane. The ambient static temperature T_∞ and pressure p_∞ are obtained using the International Standard Atmosphere (ISA) model.

The drag penalty for this system is estimated using a low-fidelity and conservative model [20] as follows:

$$D = \dot{m}_{\text{ramair}} \cdot (\eta_n \cdot v_{\text{ram,o}}), \tag{12}$$

where $\dot{m}_{\text{ramair}}$, η_n and $v_{\text{ram,o}}$ denote RA mass flow, nozzle efficiency coefficient and RA outlet velocity, respectively.

To compensate for a lack of RA created by the aircraft during take-off and landing, the fan is activated. Taking into account the fan efficiency (η_{fan}), the power electric consumption is given by:

$$\dot{W}_{\text{fan}} = \frac{\dot{m}_{\text{ramair}} \cdot \Delta p}{\rho_{\text{ram,i}} \cdot \eta_{\text{fan}}}, \tag{13}$$

Both fan and hydraulic pump mass are calculated using manufactures regression curve related to the power consumption required.

VCS The VCS is used for cooling in A1 and A2. The cycle working refrigerant is R314a. As a common VCS, the system is composed of an evaporator, a compressor, a condenser and an expansion valve and each component is modelled by the principles introduced in [22].

Using a control volume surrounding the refrigerant side of the evaporator, the heat transfer rate to the flowing refrigerant ($\dot{Q}_{\text{evap}}$) is given by:

$$\dot{Q}_{\text{evap}} = \dot{m}_{\text{ref}} \cdot (\text{h}_1 - \text{h}_4), \tag{14}$$

where $\dot{m}_{\text{ref}}$ is the refrigerant mass flow and h is the enthalpy per unit mass at each stage. The numbered subscripts are related to the station presented in Figure 1.

The refrigerant is compressed exiting the evaporator to a relatively high pressure and temperature, producing the following formula for compressor work (W_{comp}):

$$(W_{\text{comp}})_{\text{isen}} = \dot{m}_{\text{ref}} \cdot (\text{h}_{2\text{isen}} - \text{h}_1) \tag{15}$$

$$\eta_{\text{isen}} = \frac{(W_{\text{comp}})_{\text{isen}}}{(W_{\text{comp}})} = \frac{\text{h}_{2\text{isen}} - \text{h}_1}{\text{h}_2 - \text{h}_1} \tag{16}$$

where the subscript isen represents the state obtained by an isentropic evolution and η_{isen} the isentropic efficiency.

The refrigerant flows into the condenser, where the heat is transferred from the refrigerant to the RA. The rate of heat transfer ($\dot{Q}_{\text{cond}}$) is presented as,

$$\dot{Q}_{\text{cond}} = \dot{W}_{\text{comp}} + \dot{Q}_{\text{evap}} = \dot{m}_{\text{ref}} \cdot (\text{h}_2 - \text{h}_3). \tag{17}$$

Finally, in state 3, the refrigerant enters the expansion valve and expands to the evaporator pressure through a throttling procedure where:

$$\text{h}_3 = \text{h}_4. \tag{18}$$

At state 4, the refrigerant leaves the valve as a mixture of liquid and vapour.

Regarding the compressor mass, it is estimated based on component regression curves. To calculate the mass of the evaporator and condenser, as for the heat exchangers, Equations 5 and 6 are again used.

SHX The heat transferred through the SHX is modelled similarly to the approach followed for the HEX. The difference is that here the global heat transfer coefficient is calculated and the surface is a system input according to the available skin area of the aircraft (A_{SHX}). The global heat transfer coefficient neglecting the wall thermal resistance, radiation effects and fouling factors is defined in terms of convective individual heat transfer coefficients h_{ext} and h_{int}:

$$U = \frac{1}{\frac{1}{h_{\text{ext}}} + \frac{1}{h_{\text{int}}}}. \tag{19}$$

To calculate the **internal flow** convective heat transfer coefficient the following expression is used:

$$h_{\text{int}} = \frac{\kappa \cdot \overline{Nu}}{D_h}, \tag{20}$$

where $\overline{Nu}$ is the Nusselt number, D_h is the tube diameter and κ is the thermal conductivity coefficient. For a given geometry, the Nusselt number is estimated as a function of Reynolds Re_D, and Prandtl Pr numbers.

Considering a turbulent flow in circular tubes, Gnielinski provides a correlation for smooth tubes throughout a wide Reynolds number range, including the transition zone [17]:

$$Nu_D = \frac{(f/8) \cdot (Re_D - 1000) \cdot Pr}{1 + 12.7 \cdot (f/8)^{1/2} \cdot \left(P_r^{2/3} - 1\right)}. \tag{21}$$

This correlation is valid for $0.5 \leq Pr \leq 2000$ and $3000 \leq Re_D \leq 5 \cdot 10^6$. The Reynolds and Prandtl numbers are calculated in steady-state conditions using the usual relations. The friction factor f is calculated with a correlation introduced by Petukhov for a smooth surface that works for the same range of Reynolds numbers [17]:

$$f = (0.790 \cdot \ln Re_D - 1.64)^{-2} \tag{22}$$

To calculate the **external flow** convective heat transfer coefficient, some considerations are taken into account. During flight, cold ambient air adjacent to the outer surface of the aircraft increases in relation to the static temperature through ram effects [23]:

$$T_{aw} = T_\infty \cdot \left(1 + r \cdot \frac{\gamma - 1}{2} \cdot M_\infty^2\right). \tag{23}$$

The recovery factor for the turbulent boundary layer (r) is given by $r = Pr^{1/3}$, where Pr is the Prandtl number for air. T_{aw} represents the wall adiabatic temperature. Using a flat-plate analogy, the external heat transfer coefficient

may be calculated at any location on the surface of the fuselage or wing, considering a Reynolds within $10^7 < Re_X < 10^9$ [23]:

$$h_{\text{ext}} = \rho_\infty \cdot c_p \cdot v_\infty \cdot 0.185 \cdot (\log 10(Re_X))^{-2.584} \cdot Pr^{-2/3}, \tag{24}$$

where v_∞ is the aeroplane airspeed and the X in the Reynolds number denotes the distance along the fuselage/wing from its nose/leading edge to the point of interest. The aeroplane velocity can be estimated by the following expression:

$$v_\infty = M\sqrt{\gamma R T_\infty}, \tag{25}$$

with $\rho_\infty, v_\infty, \mu$ being evaluated at reference T^*:

$$T^* = \frac{T_{aw} + T_\infty}{2} + 0.22\,(T_{aw} - T_\infty)\,. \tag{26}$$

The SHX mass is calculated according to the experiment setup structure carried by Pang et al. [24]. The SHX is considered to be an aluminium block with 7.6 mm of thickness with face area equal to A_{SHX} and circular tubes with a diameter of 6 mm and a surface area equal to half of the SHX Area ($A_{\text{SHX}}/2$). The total skin heat exchanger volume is obtained by subtracting the volume of the channel from the block volume, as:

$$V_{SHX} = \left(A_{\text{SHX}} \cdot 7.6 \cdot 10^{-3}\right) - \left(\frac{A_{\text{SHX}}}{2} \cdot \frac{6 \cdot 10^{-3}}{2}\right). \tag{27}$$

The mass of the SHX may be estimated as $m_{\text{SHX}} = \rho_{\text{al}} \cdot V_{\text{SHX}}$, where ρ_{al} is the aluminium density (ρ_{SHX}).

Fuel tank The fuel tank is modelled as a control volume with fuel recirculation [14, 15]. The main governing equation of the fuel tank, following the nomenclature indicated in Figure 3, is given by:

$$\frac{dE_{cv}}{dt} = \dot{Q}_2 - \dot{Q}_1 - \dot{Q}_{\text{loss}}. \tag{28}$$

The energy of the control volume may be represented using the following equation:

$$E_{cv} = m_T \cdot c_p \cdot (T_T - T^*)\,, \tag{29}$$

where T_T and m_T represent the instantaneous temperature and mass, respectively, of the fuel in the tank. T^* is a reference temperature and c_p is again the constant-pressure specific heat of the fuel. At any given time, the temperature of the fuel coming out of the tank is the same temperature as the fuel inside the tank. The heat transfer rate $\dot{Q}_1$ is given by:

$$\dot{Q}_1 = \dot{m}_1 \cdot c_p \cdot (T_T - T^*)\,, \tag{30}$$

Additionally, $\dot{m}_1$ is the mass flow of fuel out of the fuel tank, whose value changes with the different flight phases.

After going through the wing SHX, the fuel enters the tank at a given temperature T_c. The heat transfer rate $\dot{Q}_2$ is given by:

$$\dot{Q}_2 = \dot{m}_r \cdot c_p \cdot (T_c - T^*)\,, \tag{31}$$

where m_r represents the recirculation fuel mass flow. Note that $\dot{m}_1 = \dot{m}_e + \dot{m}_r$ where $\dot{m}_e$ is the rate at which fuel is fed to the engine for propulsion purpose. $\dot{m}_e$ is related to the instantaneous fuel mass in the tank as follows:

$$\frac{dm_T}{dt} = -\dot{m}_e. \tag{32}$$

To calculate the heat loss of the fuel through the tank walls to the environment the following expression is used:

$$\dot{Q}_{\text{loss}} = U_{\text{wall}} \cdot A_{\text{wall}} \cdot (T_T - T_{aw})\,, \tag{33}$$

where U_{wall} measures the thermal resistance between the fuel all the way up to the ambient air. A reference design value for U_{wall} of 40 W/(m^{2}K) is used in the project. A_{wall} represents the portion of the tank wall both exposed to external flow and the fuel in m^2 and is estimated as follows:

$$A_{\text{wall}} = \frac{m}{m_{0,\max}} \cdot A_s + A_b. \tag{34}$$

The estimation of the side wall area of the tank A_s and the tank bottom area A_b is based on some of the initial FutPrInt50 aircraft design parameters [5].

3.4. Component model verification

Different verification methods were applied to each component to gain confidence in the simulation results. The VCS was benchmarked using the temperature–entropy (T-s) diagram of an actual VCS [22]. The counter-flow heat exchanger described was compared and verified through the typical hot and cold fluid temperature distributions associated with this type of HEX [17]. Regarding the SHX, since the modelling approach is similar to the one followed in HEX, only the variation of the external convection coefficient, which has more impact on the heat transfer, is analysed. There is no public experimental data for the SHX external heat transfer coefficient. Therefore, the model is verified using different approaches for the calculation of the heat transfer coefficient introduced by Mao et al. [6] and another semi-empirical model, from [17]. The results presented a root mean square error of 25 W/m^{2}K and 14 W/m^{2}K, respectively [6, 17]. These values are considerable when comparing to the heat transfer coefficient value (around 100 W/m^{2}K) since these are distinct semi-empirical models that had different bases in the experimental evidence. Lastly, to validate the FTMS the model introduced by Manna was replicated [15]. The results from the article (subscript a) are compared to results from this work model in Figure 4.

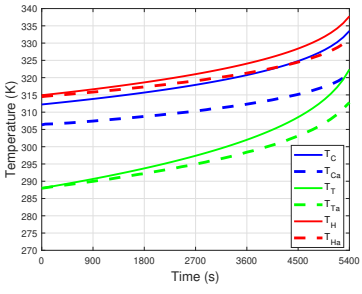

Figure 4: FTMS verification.

Although the shape of the curves is similar in both plots, the difference can be explained by the fact the

method used for the calculation of the heat transfer coefficient is not completely detailed in the aforementioned article (missing data on the flow characteristic length), as such the reference value of this work was used.

3.5. Simulation procedure

For illustrative purposes, the complete flowchart of A5 is presented in Figure 5. The simulation is done using Simulink/Matlab interface, placing each Simulink block in series taking into account the corresponding architecture layout.

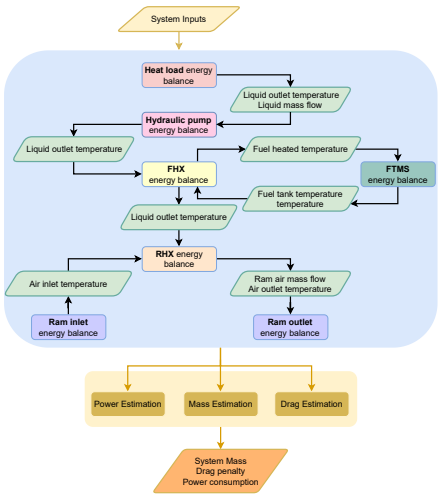

Figure 5: Architecture 5 flowchart.

3.6. Optimisation model

During the TMS conception, several variable values were estimated. Since some of them have a considerable impact on the different performance metrics, a multi-objective optimisation study was carried out. The dimension of the optimisation problem is determined by the number of design variables (x) and the challenge is to set their lower and upper limits [25]. Depending on the TMS architecture different design variables were considered including the mass flow rate of liquid and fuel, the design HEX temperature difference, the SHX area and the SHX position. The objective function $\mathrm{g}(x)$ is comprised of 3 objectives: energy consumption, total mass, and drag penalty. Thus, the TMS optimisation problem can be mathematically stated as follows:

$$\begin{aligned} &\text{minimise } \mathrm{g}(x) = [\text{Energy}\,(x)\,,\ \text{Mass}\,(x)\,,\ \text{Drag}\,(x)] \\ &\qquad\qquad\qquad\qquad \text{with respect to } x \end{aligned} \quad . \tag{35}$$

In this context, the elitist Non-dominated Sorting Genetic Algorithm (NSGA-II), as provided in [26] is used. Therefore, an optimal Pareto Front for each TMS was computed. The optimisation study continued by adding uncertainty in some variables, namely, the take-off ambient temperature and the external boundary layer thickness. Moreover, a further NSGA-II optimisation study was carried out, where the A5 was coupled with series, parallel and turboelectric propulsion models developed by Iara [27] with the goal of minimising both mass and CO_2 emissions of the combined propulsion and TMS systems.

4. Results

4.1. Baseline cases

The baseline simulation scenario is defined in Table 2.

Table 2: Conditions for the baseline scenario.

Parameter	Value/Range
Cruise altitude	7010 m
Cruise mach	0.45
Duration of flight	3600 s
Equipment waste heat load $\dot{Q}_{\text{equip}}$	100 kW
Equipment inlet temperature T_{control}	305 K
Pump/Fan efficiency η	0.5/0.4
HEX ΔT_1	10 K
Condensation Temperature T_{cond}	325.3 K
Evaporation Temperature T_{evap}	278 K
Compressor efficiency $\eta_{\text{comp}}/\eta_{\text{isen}}$	0.8/0.8
SHX Area A_{SHX}	5 m^2
Boundary layer thickness t_{bd}	0.01 m
Distance to SHX X	18/0.5750 m
Initial tank fuel temperature T_{T0}	288 K
Initial tank fuel mass m_{T0}	721 kg
Cruise mass flow of fuel $\dot{m}_e$	0.0639 kg/s
Mass flow rate of recirculation fuel $\dot{m}_r$	0.15 kg/s

4.2. Baseline results

Architectures 1 and 2 The results of the variation of the EGW temperature in different points of the liquid cooling loop are presented in Figure 6. In both cases, the equipment heat waste (100 kW) warms the EGW mixture approximately from 305 K to 312 K. In architecture 1, the evaporator will be responsible for rejecting all the heat load (green line in Figure 7) and cooling down the liquid again from 312 K until 305 K. To guarantee the VCS energy equilibrium, the heat load exchanged in the condenser is the sum of the evaporator heat transfer rate with the compressor work. In A1, the condenser heat transfer rate exchange to the RA is constant and equal to 128 kW.

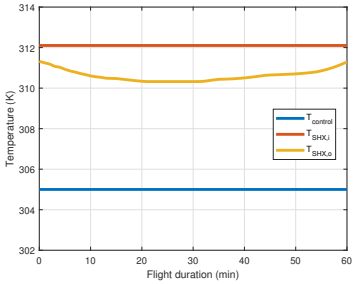

Figure 6: EGW temperature at cooling circuit points.

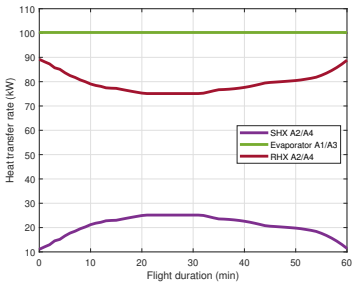

Figure 7: SHX, Evaporator and RHX heat transfer rates.

In A2, the heat transfer rates in the different stations will vary since the system behaviour depends on the ambient temperature used to cool the liquid in SHX. The SHX cooling capacity is higher during cruise, with 25% of the heat being rejected through it in this phase as

confirmed by the purple curve in Figure 7. This is due to the lower ambient air temperature. Thus, the SHX liquid outlet temperature is also lower in cruise (CR) (yellow curve in Figure 6). The variation of the heat transferred to the VCS through the evaporator (red curve in Figure 7) is the opposite of the variation of the heat transfer rate across SHX since the sum of both results is the total heat load that enters the system. This way, the heat rejected to VCS is at its minimum during cruise as well as the required compressor work and the heat rejected at the condenser.

Due to the favourable cooling properties of RA during CR, less mass flow is required, setting Take-Off (TO) and Landing (L) as the critical points in terms of ram inlet flow in both cases (Figure 8). The RA mass flow required is higher in case 1 (green line) because more heat is transferred at the condenser level. Regarding the fan, this device is only used during TO and L to ensure that the required mass flow of RA enters the aircraft. The fan work is 2 kW higher in case 1 (15 kW) when compared to case 2 (13 kW) since more RA mass flow needs to be pulled. About the electric consumption of the hydraulic pump, the pressure drop through the liquid cooling loop is roughly estimated so the value is only indicative and used for comparisons. In this case, the pump work required is higher in case 2 (approximately 0.5 kW) due to the fact that more heat transfer stations are considered, namely, the SHX, resulting in a greater pressure drop.

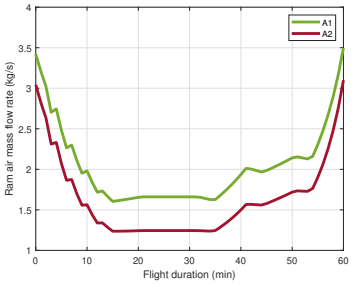

Figure 8: Ram air mass flow rate.

Architectures 3 and 4 As mentioned before, A3 basically corresponds to A1 but replaces the VCS with a RHX, while A4 matches A2 but again replacing VCS with a RHX. Using the same operating conditions, the SHX in A4 will have the same behaviour and effect in the system as in A2. This way, both $\dot{Q}_{\mathrm{SHX}}$ and the evolution of EGW temperature in the circuit are the same as portrayed in Figures 6 and 7. Also, the variation in the RHX heat transfer rate for both A3 and A4 is the same as described at the evaporator level for A1 and A2, respectively. The difference is that instead of having an evaporator rejecting heat to a refrigerant and, only then, a condenser rejecting heat to a ram air flow, in A3 and A4, the heat is rejected directly to the RA.

The RA mass flow required during TO and L for A3 and A4 is approximately 11 kg/s. Since the heat exchangers were designed to guarantee a 10 K difference between the outlet air temperature and the inlet fluid temperature, the hotter the inlet fluid is, the hotter the RA can exit the RHX. Besides the larger heat transfer rate transferred to the RA in A1 and A2, the higher air outlet temperature, due to the large R314a condensation temperature (325.3 K), leads to a lower mass flow rate required when compared to the A3 and A4. The fan in A3 and A4 also has a similar response as described for A1 and A2 but with greater magnitudes of work required.

Architecture 5 Since the equipment heats the EGW mixture from 305 K until 312 K, the heated fuel temperature is approximately 302 K according to ΔT_1=10 K (orange line in Figure 9). After passing through the fuel heat exchanger, the recirculation fuel is cooled through a SHX. Again, as in the previous cases, since the outside air temperature is lower at the cruise phase, the SHX cooling capacity is at its maximum during CR and the temperature of the cooled fuel will be lower in CR (yellow line in Figure 9). $\dot{Q}_{\mathrm{SHX}}$ is lower in A5 (3 kW in TO and 12 kW in CR), first, because the SHX fuel inlet temperature is lower than the SHX EGW inlet temperature, and second, due to the fact that the fuel specific heat at constant pressure and mass flow rate are smaller when comparing to the EGW scenario.

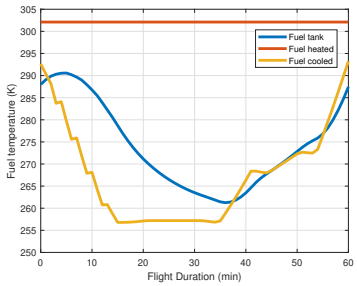

Figure 9: Fuel temperature at different circuit points.

The recirculation fuel temperature will decrease until the cruise phase is reached, so the fuel temperature in the tank (blue line in Figure 9) is also expected to decrease. The first initial increase described by the blue line can be attributed to two factors. On the one hand, in the first flight section, the outside air temperature is higher than the fuel temperature, and on the other hand, the temperature of the cooled fuel is superior to the initial temperature of the fuel in the tank. After the CR and with the altitude decrease, the outside air temperature increases having an effect on both tank heat losses and SHX heat transfer rate and leading to an increase in the fuel tank temperature until the end of the flight.

Since the inlet temperature and the mass flow rate of the EGW mixture through the FHX is constant, the heat transferred in this section only depends on the fuel temperature in the tank and the fuel mass flow. The decrease of the fuel temperature in the tank until the end of CR potentiates the heat transfer, and although when passing to the cruise phase the mass flow rate of fuel decreases, the heat transfer rate continues to increase. Then, the fuel temperature in the tank starts to increase during the descent phase and there is a massive break in the fuel mass flow which causes the FHX heat transfer rate to decrease and a visible peak of the heat transfer rate at approximately 35 minutes after take-off as highlighted by Figure 10.

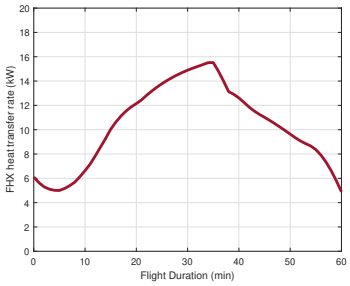

Figure 10: FHX heat transfer rate.

To dissipate the constant heat load to the EGW mixture, the heat exchange in RHX exhibits the reverse behaviour of the FHX with a minimum peak of around 84 kW at 35 minutes of flight. It is also worth to note that the heat transfer rate required from the RHX is decreasing at CR, the same phase where the ambient air conditions are favourable to the heat transfer given the low ambient air temperature. This way, the ram air mass flow required to cool the liquid mixture is low during CR (2 kg/s). The fan consumes approximately 47.822 kW during TO and L. The fuel pump consumption value is also estimated to be around 3.220 kW throughout the whole flight.

Impact of the baseline results Table 3 presents the total mass, drag and power consumption impacts of each architecture. The **total mass** of each architecture is estimated by summing each contributing component mass. The heat exchangers mass values obtained for the baseline operating conditions range from 5 kg to 20 kg depending on their heat transfer rate and on the type of heat exchanger considered. Regarding the SHX mass, its value of 80.74 kg is slightly higher than what was expected because its calculation is based on a experimental construction (not embedded in the aircraft frame) [6]. As far as the power consumption elements are concerned, the fan used to pull the RA has the largest penalty impact (90 kg). From Table 3, the final mass values indicate that architecture 5 is the heaviest one (596.208 kg), because it adds the fuel recirculation pump and has three heat exchangers (FHX, SHX and RHX). The difference between the mass of A1 and A2 is justified by the SHX addition, and the same applies to the difference between A3 and A4.

Regarding the **electric energy consumption**, A1 and A2 have the highest energy impact (around 200 MJ) since they have three duplicated electric components: the compressor, the fan and the hydraulic pump. A5 also has a considerable energy consumption (32.511 MJ) due to the fuel recirculation pump.

In this work context, the **drag penalty** is directly related to the RA required at the RHX level. As during the take-off and landing the mass flow is higher, the expected drag is also superior in TO and L when compared to the cruise phase. The larger drag penalty values are associated with superior RA mass flow estimations.

4.3. Parametric study

A parametric study has been conducted to investigate the sensitivity of TMS architectures with a selection of different operating conditions including the liquid mass flow rate, the SHX area, the SHX position, the designed temperature difference for HEX, the recirculation mass flow rate of fuel and the tank parameters. Some relevant results are presented in Table 4. The most important conclusion from this parametric study is that only the SHX area had the reverse effect on the analysed metrics: by increasing the skin heat exchanger area, the mass would increase, but both drag and energy consumption would decrease. With that said, all the design variables except the A_{SHX} tend to one of the limits of the range considered. Consequently, Pareto fronts presented in Section 4.4 are mostly influenced by A_{SHX}.

4.4. Optimisation results

A 3-D Pareto front was obtained for A2, A4 and A5. For sake of brevity, only plots of 2D slices of the 3D problem results for cases 2 and 4 are presented in this section.

The trade-off in the optimal layouts is the one expected. Looking at Figure 11, and according to Table 3, A2 (identified by the red colour) can reach lower values of drag penalty for some design layouts, but has a much superior energy consumption. The mass-drag 2D Pareto detailed that A4 can be lighter but with a higher drag penalty when compared to A2. The Pareto in terms of mass and energy consumption also validated the previous results by showing that, in terms of mass, A4 can reach lower values for much lower energy consumption. Therefore, the use of A4 to dissipate the heat from HEP waste heat seems to be advantageous in terms of mass and energy consumption but creates a larger RA drag.

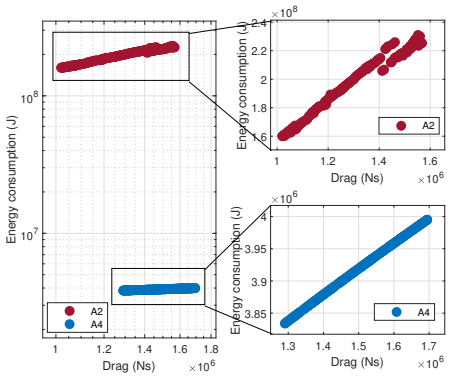

Figure 11: Pareto fronts for drag penalty and energy consumption.

Table 3: Total mass, drag and power consumption of each TMS.

Results	A1	A2	A3	A4	A5
Mass (kg)	388.157	536.936	396.797	556.713	596.208
Energy consumption (MJ)	261.575	207.833	9.077	9.245	32.511
CR Drag penalty (N)	255.267	191.291	297.916	230.950	263.448
TO Drag penalty (N)	297.711	264.916	871.209	843.582	856.549

Table 4: Summary of the most important results from the parametric study.

Variable	Total mass [kg]	Energy consumption [MJ]	Max. Drag penalty [Ns]
↓ EGW mass flow rate (A2)	↓ 14%	↓ 4%	↓ 4%
↑ SHX area (A4)	↑ 12%	↓ 0.6%	↓ 12%
↓ SHX fuselage/wing position (A4)	↓ 0.3%	↓ 0.3%	↓ 0.6%
↓ HEX temperature difference (A5)	↓ 9%	↓ 6%	↓ 30%
↓ Recirculation fuel mass flow (A5)	↑ 0.54%	↑ 23%	↓ 2%

Then, uncertainty was added to the air temperature at TO and external boundary layer thickness for the same objective function. As predicted, since the design is more robust, i.e, less sensitive to inherent variability, the maximum values obtained in the three domains were higher when compared to the deterministic results.

A further optimisation analysis coupling series, parallel and turboelectric HEP computational models with A5 was also conducted. The results are shown in Figure 12.

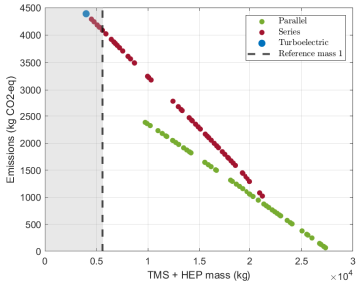

Figure 12: Pareto fronts for HEP and A5.

To explain the overall Pareto behaviour, it is worth mentioning that the battery has the largest influence in terms of mass, while the fuel flowing to the combustion engine has the largest influence in terms of CO_2 emissions. Although the parallel powertrain is preferable when compared to the series case in terms of emissions, it has a higher mass penalty. According to the parallel architecture electrical branch chain, the power required to the battery pack is higher than for the series case. This way, the system will be heavier for all the hybridisation factors and the turboshaft will be downsized leading to fewer emissions. The turboelectric architecture is similar to the series architecture but does not include a battery in the powertrain. When comparing the turboelectric case and the lowest hybridisation factor series case, it can be seen that the CO_2 emissions and the overall mass are identical. This is because the series case for a hybridisation factor of 0% corresponds to the turboelectric architecture. An important reference mass was added to this analysis indicating a mass of a conventional propulsion system based on a similar aircraft (ATR42-600). Even though the zone on the right side of the reference line gives ambitious values of CO_2 emissions by increasing the power required by the battery, it yields unrealistic values in terms of the maximum propulsive mass. Only the series architecture can reach the realistic zone for hybridisation factors ranging between 0 and 9%. This outcome alerts to the need for more technological progress to enable flight electrification of regional aeroplanes.

5. Conclusions

As electric propulsion becomes more common, thermal management is expected to become a major design concern for next-generation aircraft. In this work, five distinct TMS were developed, all of which making use of the two primary heat sinks that were found in the literature (the atmospheric air and the fuel). The systems are analysed according to the heat transfer rate potential and the temperatures of the managed fluids at each heat sink. A heat sink will be preferable if it has a high cooling capacity while having a low mass, drag, and power impact.

Some comments about the primary heat sinks are worth to consider. **Fuel** is one of the primary heat sinks although its cooling capacity is limited by the weight of the tank. It will be challenging to achieve cooling needs since the trend toward less on-board fuel and higher thermal loads raises various safety concerns. **RA** has a considerable cooling capability. Depending on the thermal loads being dissipated, it will impose an extra drag penalty. The initial mass flow needed to cool the load discussed in this work is too large for the current generation of RHX to handle and a rearrangement of tinier RHXs is required. **SHX** is an inadequate solution on its own due to size and cooling space constraints in the fuselage and wing for the mission here considered. It would be more efficient for long and medium distance flights with extended cruising phases. At the same time, the introduction of composite materials in aircraft structures has decreased the likelihood of removing excess heat through the aeroplane skin since composites have lower heat conductivities than metallic materials.

A parametric study was also implemented, which gave a sensitivity analysis of the design factors to improve each architecture performance. With the insights from the parametric study, a multi-objective optimisation to minimise TMS drag, weight, and energy consumption using a genetic algorithm was also formulated.

Finally, it was found that none of the investigated architectures performs ideally across all of the studied metrics. Thus, when designing the TMS for future HEA, different architectures must be analysed and the different objective functions must be evaluated so they can be prioritised according to the different power requirements and design needs. The direct integration in early design phases of the TMS and HEP system, as followed in the last optimisation study of this research, is thus of extreme importance to study the feasibility of this aircraft concept. Moreover, multidisciplinary analyses also addressing aerodynamics and structures in a synergistic way should be done to decrease fuel dependency without losing performance.

References

[1] European Commission. *Flightpath 2050 vision for European aviation.* Publications Office of the Euro-

pean Union, Luxembourg, 2011. ISBN 978-92-79-19724-6.

[2] F. Afonso, M. Sohst, C. M. A. Diogo, S. S. Rodrigues, A. Ferreira, I. Ribeiro, R. Marques, F. F. C. Rego, A. Sohouli, J. Portugal-Pereira, H. Policarpo, B. Soares, B. Ferreira, E. Fernandes, F. Lau, and A. Suleman. Strategies towards a more sustainable aviation: a systematic review. Submitted to *Progress in Aerospace Sciences*, 2022.

[3] A. van Heerden, D. Judt, S. Jafari, C. Lawson, T. Nikolaidis, and D. Bosak. Aircraft thermal management: Practices, technology, system architectures, future challenges, and opportunities. *Progress in Aerospace Sciences*, 128:100767, 2022. doi:10.1016/j.paerosci.2021.100767.

[4] W. Affonso, R. Gandolfi, R. J. N. dos Reis, C. R. I. da Silva, N. Rodio, T. Kipouros, P. Laskaridis, A. Chekin, Y. Ravikovich, N. Ivanov, L. Ponyaev, and D. Holobtsev. Thermal management challenges for HEA – FUTPRINT 50. *IOP Conference Series: Materials Science and Engineering*, 1024(1):012075, 2021. doi:10.1088/1757-899x/1024/1/012075.

[5] N. Moebs, D. Eisenhut, E. Windels, J. van der Pols, and A. Strohmayer. Adaptive Initial Sizing Method and Safety Assessment for Hybrid-Electric Regional Aircraft. *Aerospace*, 9(3):150, 2022. doi:10.3390/aerospace9030150.

[6] Y.-F. Mao, Y.-Z. Li, J.-X. Wang, K. Xiong, and J.-X. Li. Cooling Ability/Capacity and Exergy Penalty Analysis of Each Heat Sink of Modern Supersonic Aircraft. *Entropy*, 21(3):223, 2019. doi:10.3390/e21030223.

[7] B. T. Schiltgen and J. Freeman. Aeropropulsive Interaction and Thermal System Integration within the ECO-150: A Turboelectric Distributed Propulsion Airliner with Conventional Electric Machines. In *16th AIAA Aviation Technology, Integration, and Operations Conference*, Washington, DC, USA, June 2016. doi:10.2514/6.2016-4064.

[8] J. W. Chapman, H. Hasseeb, and S. L. Schnulo. Thermal Management System Design for Electrified Aircraft Propulsion Concepts. In *AIAA Propulsion and Energy 2020 Forum*, (Virtual Event), August 2020. doi:10.2514/6.2020-3571.

[9] E. Sozer, D. Maldonado, K. Bhamidapati, and S. L. Schnulo. Computational Evaluation of an OML-based Heat Exchanger Concept for HEATheR. In *AIAA Propulsion and Energy 2020 Forum*, (Virtual Event), August 2020. doi:10.2514/6.2020-3575.

[10] N. Heersema and R. Jansen. Thermal Management System Trade Study for SUSAN Electrofan Aircraft. In *AIAA SCITECH 2022 Forum*, San Diego, CA, USA, January 2022. doi:10.2514/6.2022-2302.

[11] M. Shi, M. Sanders, A. Alahmad, C. Perullo, G. Cina, and D. N. Mavris. Design and Analysis of the Thermal Management System of a Hybrid Turboelectric Regional Jet for the NASA ULI Program. In *AIAA Propulsion and Energy 2020 Forum*, (Virtual Evente), August 2020. doi:10.2514/6.2020-3572.

[12] H. Kellermann, M. Lüdemann, M. Pohl, and M. Hornung. Design and Optimization of Ram Air–Based Thermal Management Systems for Hybrid-Electric Aircraft. *Aerospace*, 8(1):3, 2021. doi:10.3390/aerospace8010003.

[13] H. Kellermann, A. Habermann, P. Vratny, and M. Hornung. Assessment of fuel as alternative heat sink for future aircraft. *Applied Thermal Engineering*, 170:114985, 2020. doi:10.1016/j.applthermaleng.2020.114985.

[14] L. Pang, S. Li, M. Liu, R. A, A. Li, and F. Meng. Influence of the Design Parameters of a Fuel Thermal Management System on Its Thermal Endurance. *Energies*, 11(7):1677, 2018. doi:10.3390/en11071677.

[15] R. Manna, N. Ravikumar, S. Harrison, and K. Goni Boulama. Aircraft Fuel Thermal Management System and Flight Thermal Endurance. *Transactions of the Canadian Society for Mechanical Engineering*, 46(2), 2022. doi:10.1139/tcsme-2021-0146.

[16] I. Abrantes, A. F. Ferreira, A. Silva, and M. Costa. Sustainable aviation fuels and imminent technologies - CO2 emissions evolution towards 2050. *Journal of Cleaner Production*, 313:127937, 2021. doi:10.1016/j.jclepro.2021.127937.

[17] F. P. Incropera and D. P. DeWitt. *Fundamentals of Heat and Mass Transfer*. John Wiley & Sons, New York City, New York, 7th edition, 2011.

[18] AC-9 Aircraft Environmental Systems Committee. Heat Sinks for Airborne Vehicles, December 2021.

[19] J. E. Hesselgreaves, R. Law, and D. A. Reay. Chapter 4 - surface comparisons, size, shape and weight relationships. In J. E. Hesselgreaves, R. Law, and D. A. Reay, editors, *Compact Heat Exchangers*, pages 129–155. Butterworth-Heinemann, second edition, 2017. doi:10.1016/B978-0-08-100305-3.00004-5.

[20] R. Larkens. A coupled propulsion and thermal management system for hybrid electric aircraft design: A case study. MSc in Aerospace Engineering, Delft University of Technology, 2020.

[21] Philip G. Hill e Carl R. Peterson. *Mechanics and Thermodynamics of Propulsion*. Addison-Wesley Publishing Company, 2nd edition, 1992.

[22] M. Moran, H. Shapiro, D. Boettner, and M. Bailey. *Fundamentals of Engineering Thermodynamics*. Wiley, 2010. ISBN 9780470495902.

[23] American Society of Heating Refrigerating and Air-Conditioning Engineers. *ASHRAE Handbook: Heating Ventilating and Air-Conditioning Applications SI Edition*. 2015.

[24] L. Pang, X. Dang, and J. Cheng. Study on Heat Transfer Performance of Skin Heat Exchanger. *Experimental Heat Transfer*, 28(4):317–327, 2015. doi:10.1080/08916152.2013.876461.

[25] J. R. R. A. Martins and A. Ning. *Engineering Design Optimization*. Cambridge University Press, 2021. ISBN 9781108833417. doi:10.1017/9781108980647.

[26] A. Seshadri. NSGA - II: A multi-objective optimization algorithm. `https://tinyurl.com/3y5avp9h`, 2022. Accessed: 2022-07-15.

[27] I. A. A. Figueiras. Development of computational models for hybrid-electric propulsive systems. MSc Thesis in Aerospace Engineering, Instituto Superior Técnico, Lisbon, Portugal, 2022.